

A kinetic-optimized CoChR variant with enhanced high-frequency spiking fidelity

Xiaoke Bi,^{1,*} Connor Beck,¹ and Yiyang Gong^{1,*}

¹Department of Biomedical Engineering, Duke University, Durham, North Carolina

ABSTRACT Channelrhodopsins are a promising toolset for noninvasive optical manipulation of genetically identifiable neuron populations. Existing channelrhodopsins have generally suffered from a trade-off between two desired properties: fast channel kinetics and large photocurrent. Such a trade-off hinders spatiotemporally precise optogenetic activation during both one-photon and two-photon photostimulation. Furthermore, the simultaneous use of spectrally separated genetically encoded indicators and channelrhodopsins has generally suffered from non-negligible crosstalk in photocurrent or fluorescence. These limitations have hindered crosstalk-free dual-channel experiments needed to establish relationships between multiple neural populations. Recent large-scale transcriptome sequencing revealed one potent optogenetic actuator, the channelrhodopsin from species *Chloromonas oogama* (CoChR), which possessed high cyan light-driven photocurrent but slow channel kinetics. We rationally designed and engineered a kinetic-optimized CoChR variant that was faster than native CoChR while maintaining large photocurrent amplitude. When expressed in cultured hippocampal pyramidal neurons, our CoChR variant improved high-frequency spiking fidelity under one-photon illumination. Our CoChR variant's blue-shifted excitation spectrum enabled simultaneous cyan photostimulation and red calcium imaging with negligible photocurrent crosstalk.

SIGNIFICANCE Channelrhodopsins are tools that can target optical manipulation to neuron populations. Existing channelrhodopsins have suffered from a trade-off between two properties, fast channel kinetics and large photocurrent. The simultaneous use of spectrally separable genetically encoded indicators and channelrhodopsins have generally suffered from non-negligible photocurrent or optical crosstalk, which generate unwanted neuron depolarization or crosstalk fluorescence transients. These limitations have hindered spatiotemporally precise neuron activation and dual-channel experiments that elevate neural circuit dissection. To address these limitations, we used rational design to generate multiple CoChR variants with high cyan-light-driven photocurrent. Our best variant exhibited accelerated channel kinetics while maintaining large photocurrent amplitude. These properties could allow our CoChR variant to serve as a tool in future high-frequency or dual-channel neuroscience experiments.

INTRODUCTION

Mammalian brains support sophisticated mental and behavioral tasks within diverse and complex neural circuits. Neural circuit elements are often a population of genetically identifiable neurons that carries out one physiologically or behaviorally relevant function when activated or suppressed. To untangle the complexity and diversity of such underlying neural circuit elements, neuroscientists have developed a toolset that precisely examines the contributions of specific neuron types

in vivo. One portion of this toolset is genetically encoded indicators and optogenetic actuators; they can record or modulate neural activity, respectively, with genetic specificity.

The channelrhodopsin is a class of optogenetic actuator widely used to modulate neural activity (1–4). Simultaneous optogenetic stimulation of one neural population and electrophysiological or behavioral readouts have revealed functional connectivity of complex neural circuits *in vitro* and *in vivo* (2,3,5–7). For example, simultaneous photostimulation of axons expressing Channelrhodopsin-2 (ChR2) and whole-cell recording of synaptic current assisted the circuit mapping of long-range callosal projection from mouse somatosensory cortex (8). Direct manipulation of neural activity using ChR2 in live mice revealed an odor processing

Submitted January 19, 2022, and accepted for publication September 21, 2022.

*Correspondence: xiaoke.bi@duke.edu or yiyang.gong@duke.edu

<https://doi.org/10.1016/j.bpj.2022.09.024>

© 2022 Biophysical Society.

mechanism in the bulbar-cortical circuit of the olfactory system (9).

The neuroscience community now aspires toward multi-channel experiments with combinations of simultaneous optogenetic stimulation or imaging of neural activity. Such dual-channel experiments, when combined with complementary methodologies in system neuroscience, are crucial for probing interactions between different populations of neurons (2,3,10–15). For example, time-locked simultaneous optogenetic manipulation of different neuron populations revealed that increased inhibitory input could partially rescue social behavior disruption caused by elevated excitation/inhibition imbalance (16). Simultaneous optogenetic perturbation of presynaptic terminals and calcium imaging of neural activity in downstream cell bodies identified a direct projection from the prefrontal cortex to the hippocampus that mediated contextual memory retrieval (17).

Previous implementation of simultaneous optical imaging and optogenetic stimulation using ChR2 exhibited unwanted neuron depolarization by the imaging light or large optical artifacts in the imaging channel. One-photon photostimulation generated large optical artifacts due to spectral overlap between ChR2's excitation spectrum and the protein sensor's excitation spectrum. This required discarding optical data or blocking the imaging channel during photostimulation (18,19). This limitation was addressed by using two-photon excitation with a red-shifted C1V1 light-activated channel and the green calcium indicator GCaMP6s (20,21). The C1V1 excitation wavelength minimally overlapped with the GCaMP6s excitation spectrum and thus effectively reduced the optical artifact (22). However, the imaging light still generated non-negligible depolarizing photocurrent due to spectral overlap between the two-photon imaging wavelength and the two-photon C1V1 excitation spectrum (21). Such unwanted depolarization hindered temporally precise control of neuron activities with optogenetic stimulation. Lower imaging excitation power mitigated unwanted depolarization, but could constrain the shot noise-limited imaging quality.

Modern engineering strategies have partially reduced optical and photocurrent crosstalk in dual-channel experiments by improving the spectral separability between genetically encoded indicators and optogenetic actuators. These strategies either pushed the indicators toward red or near-infrared (NIR) wavelengths, or pushed the actuators toward blue wavelengths (11,23–29). One recent large-scale transcriptome sequencing screen generated a potent channelrhodopsin from the species *Chloromonas oogama* (CoChR) (30) that could potentially fit into dual-channel experiments; this rhodopsin had a blue-shifted action spectrum and large photocurrent. However, CoChR's slow off-kinetics could compromise the temporal precision of light activation and limit the firing frequency in both one-photon and two-photon photostimulation applications.

In this study, we sought to optimize the channel kinetics of CoChR such that it could enable high temporal precision in one-photon optogenetics. Targeted mutations to ChR2 have already improved channel kinetics and the temporal resolution of neuron activation (30–32). For example, rational engineering of the electronic environment surrounding the retinal Schiff base (RSB) of ChR2 resulted in ChETA_T, which drove precisely timed spikes up to 200 Hz (31). Rational design further expanded the ChETA family by introducing additional mutations around the ion pore or on the third or fourth helices surrounding the RSB, resulting in ChETA_{TR}, ChETA_A, ChETA_{AR}, and ChETA_{TC}. These ChETAs demonstrated faster channel deactivation and recovery than native ChR2 (32,33). Such capabilities were valuable in neuroscientific research involving fast-spiking interneurons and induction of plasticity (34,35). However, an inverse relationship typically governed the trade-off between fast kinetics and high photocurrent (36,37): fast channelrhodopsins often had low photocurrent amplitude. To circumvent such a trade-off, previous engineering strategies combined multiple single-amino-acid substitutions in ChR2 and obtained combinatorial effects (32,38).

Given the homology between ChR2 and CoChR, we hypothesized that some homologous combinations of ChR2's mutations increasing kinetics could also speed up CoChR's kinetics and maintain or increase CoChR's photocurrent. We rationally designed 11 CoChR variants with either single amino-acid substitutions or combinations of substitutions based on homology with ChR2. We found a kinetic-optimized CoChR variant, CoChR (H94E/E103A), which demonstrated high spiking fidelity in response to high-frequency photostimulation in cultured hippocampal pyramidal neurons. Our CoChR (H94E/E103A) also enabled low-crosstalk dual-channel experiments with concurrent red-fluorescence calcium imaging of jRCaMP1b and complementary optical design.

MATERIALS AND METHODS

Plasmid construction

We constructed all CoChR-EGFP variant plasmids using site-directed mutagenesis and two-step PCR to introduce single-amino-acid substitutions on wild-type CoChR. CheRiff, ChrimsonR, Chronos, and ChroME used for benchmarking comparison were subcloned from Addgene plasmids #51693, #59049, #80902, and #108902, respectively. All constructs were expressed in a lentivirus backbone under the CamKII α promoter.

Cell cultures

HEK293T cells were cultured in Dulbecco's modified Eagle's medium (DMEM) (#10569010; Gibco, Waltham, MA) supplemented with 10% fetal bovine serum (FBS) (#16000044; Gibco) and 1% streptomycin (#15070063; Gibco). We delivered plasmids into HEK293T cells using chemical transfection for kinetic and photocurrent characterization. We transfected HEK293T cells with Lipofectamine 2000 (#11668019;

Invitrogen, Waltham, MA) 1–2 days after passaging and imaged them 1 day post transfection.

All animal handling and imaging procedures were performed according to protocols approved by the Duke Institutional Animal Care and Use Committee. We dissected rat hippocampal neurons from postnatal day 0 Sprague-Dawley pups (Charles River Labs, Chapel Hill, NC) and cultured them in Neurobasal Media A (#10888022; Gibco) supplemented with GlutaMAX (#A1286001; Gibco) and B-27 Supplement (#17504044; Gibco). We transfected neurons using calcium phosphate 3 days after plating. We then imaged and patched these neurons 3–5 days post transfection.

Electrophysiology

We applied various light pulses to whole-cell patched HEK293T cells and cultured rat hippocampal neurons, and we recorded photocurrent and photovoltage using an Axon Digidata 1550A (Axon Instruments, San Jose, CA) digitizer, Multiclamp 700A amplifier (Axon Instruments), and pClamp (version 7.1) software. In HEK293T cells, we applied 5 ms light pulses at 1 Hz and 1 s light pulses at 0.5 Hz to measure the peak photocurrent and steady-state photocurrent, respectively, at a -50 mV holding potential in voltage clamp. In cultured neurons, we applied 5 ms light pulses at 1 Hz to measure the photocurrent, at a -50 mV holding potential in voltage clamp. We applied 5 ms light pulses at 10, 16, 20, 25, and 32 Hz to elicit action potentials under current clamp.

All samples were mounted in a perfusion chamber in which the extracellular medium was kept at 22°C and consisted of 150 mM NaCl, 4 mM KCl, 10 mM glucose, 10 mM HEPES, 2 mM CaCl_2 , and 2 mM MgCl_2 . The intracellular solution contained 129 mM K-gluconate, 10 mM KCl, 10 mM HEPES, and 4 mM Na_2ATP .

Optics

We used a $40\times/0.8$ numerical aperture water immersion objective (Nikon, Tokyo, Japan) for all imaging experiments. To photostimulate and image CoChR variants tagged by EGFP, we used a 490 nm LED (M490L4; Thorlabs, Newton, NJ) with an intensity of 1 mW/mm^2 at the sample plane and a Nikon B-2E/C filter cube containing a 475/28 nm excitation filter (FF01-475/28-25; Semrock, Rochester, NY), a 505 nm long-pass dichroic mirror (T505lpxr; Chroma, Bellows Falls, VT), and a 535/40 nm emission filter (D535/40m; Chroma).

For simultaneous dual-channel imaging experiments, we used the same 490 nm LED as above to photostimulate CoChR variants and a 595 nm LED (M595L4; Thorlabs) to image jRCaMP1b. These LEDs passed through a 475/28 nm excitation filter and a 585/11 nm excitation filter, respectively and then combined at a 552 nm long-pass dichroic mirror (FF552-Di02; Semrock). The excitation path after this dichroic mirror contained a 505 nm long-pass dichroic mirror (T505lpxr; Chroma) and a 593 nm long-pass dichroic mirror (FF593-Di03; Semrock) to reflect cyan and orange excitation light onto the sample plane, respectively. The cyan light intensity was 1 mW/mm^2 or 3 mW/mm^2 at the sample plane, while the orange light intensity was 0.5 mW/mm^2 at the sample plane. Emitted red fluorescence passed through a 641/75 nm emission filter (FF01-641/75-25; Semrock). We imaged neurons at 10 Hz using an sCMOS camera (OptiMOS; QImaging, Tuscon, AZ).

Electrostatic potential calculation

We simulated protein structures using AlphaFold (version 2.0) (39) with sequence information (Table S1). We converted the output PDB file into a PQR file using the DB2PQR tool (40) on the Poisson-Boltzmann web server (<https://server.poissonboltzmann.org/>). We used CHARMM as force field (41). We calculated electrostatic potential surfaces on the output PQR file using APBS (1.4) through its plugin in VMD (version 1.9.4a55) (42).

Data analysis

Off-kinetics calculation

We characterized the off-kinetics of all CoChR variants and native CoChR by their decay time constants of photocurrent generated by 5 ms light pulses. We fitted the decay phase of photocurrent generated by 5 ms light pulses with an exponential function:

$$I(t) = I_0 e^{-(t-t_0)/\tau} + I_{\infty},$$

where $I(t)$ represented the photocurrent as a function of time, t represented the time, I_0 represented the peak photocurrent, t_0 represented starting time for fitting, I_{∞} represented the baseline current, and τ represented the decay time constant of photocurrent.

Photocurrent amplitude normalization

We defined the peak photocurrent amplitude as the difference between the baseline current and the maximum photocurrent generated by a 5 ms light pulse. We defined the steady-state photocurrent amplitude as the difference between the baseline current and the plateau photocurrent generated by 1 s light illumination. We then normalized the peak and steady-state photocurrent amplitude with both membrane capacitance and fluorescence to counteract the effect of cell size and expression level on photocurrent amplitude, respectively. For comparisons between CoChR variants, we also normalized the peak and steady-state photocurrent amplitude of each CoChR variant to the average peak and steady-state photocurrent amplitude of native CoChR, respectively.

To measure the membrane capacitance, we applied a -20 mV test voltage relative to the holding voltage for 100 ms at the start of photostimulation protocols. We fitted the current transient with the same exponential function as the one used for measure decay kinetics; the baseline current was now the steady-state current in response to the voltage step. R_a and R_m represented pipette resistance and membrane resistance, respectively, and were calculated with equations

$$R_a = \frac{V_c}{I_0},$$

$$R_m = \frac{V_c}{I_{\infty}} - R_a,$$

where V_c represented the clamp voltage. We then calculated membrane capacitance C_m using the equation

$$C_m = \tau \left(\frac{1}{R_m} + \frac{1}{R_a} \right).$$

To quantify the fluorescence level, we took fluorescence images of HEK293T cells using 1 mW/mm^2 light density and 1000 ms exposure time. The fluorescence images were processed sequentially with MATLAB functions *graythresh*, *imbinarize*, *bwboundaries*, *edge*, and *imdilate* to obtain spatial masks over the boundaries of the cell membrane. We then multiplied masks with the raw fluorescence images and aggregated all intensity values to obtain the fluorescence level.

50% spiking probability calculation

We characterized the 50% spiking probability of each neuron measurement by fitting its spiking probability versus stimulation frequency curve with the Hill equation:

$$P(f) = \frac{1}{1 + a(f - f_0)^n},$$

where P represented the spiking probability and f represented the stimulation frequency. a , f_0 , and n were three fitting parameters, where f_0 represented the start point of fitting (lowest stimulation frequency).

Plateau potential calculation

We defined the plateau potential as the average membrane voltage of the late falling phase of action potentials in the last half of the inter-photostimulation interval.

Transient optical artifact removal

Because we used a cyan light stimulation protocol that contained a train of three pulses (5 ms width) at 25 Hz, the stimulation was limited to single imaging frames (100 ms). We removed these individual frames containing the transient optical artifacts for later $\Delta F/F$ calculation.

$\Delta F/F$ calculation

We defined $\Delta F/F$ as the difference between the jRCaMP1b fluorescence during applied trains of photostimulation and at rest. After removing frames containing the transient optical artifacts, we first summed remaining frames to generate a total image. To calculate the $\Delta F/F$, we generated masks by processing this total image using MATLAB functions *graythresh* and *imbinarize* in sequence. We then applied the masks to each frame of the raw fluorescence videos to obtain the fluorescence trace. We calculated the baseline fluorescence by averaging the fluorescence in the first 10 frames, which was before the first trains of photostimulation.

RESULTS

Target mutations around the ion pore and RSB enhanced photocurrent and channel kinetics of CoChR

We targeted five amino acid residues in CoChR that were homologous to residues altering channel kinetics or photocurrent in ChR2 (Fig. 1). Single-amino-acid substitutions at these homologous residues in ChR2 generated two classes of optogenetic function; one class enhanced maximal photo-

current amplitude (TC, CatCh, and ChR2_R) while the other class accelerated off-kinetics (ChETA_T and ChETA_A). These residues were respectively located near the ion pore (Fig. 1, *a* and *b*) or on the third or fourth helices surrounding the RSB (Fig. 1, *a* and *c*).

Single-amino-acid substitutions on the targeted residues accelerated the off-kinetics or enhanced the photocurrent of CoChR in response to 475 nm light (Fig. 2; materials and methods). Like other depolarizing channelrhodopsins, CoChR and its variants under constant illumination generated photocurrent traces that consist of a peak followed by a lower plateau (Fig. 2 *a*). Next, we characterized the off-kinetics, normalized peak, and steady-state photocurrent amplitudes of the variants (Figs. 2, *b* and *c* and S1; materials and methods). CoChR (E103T) and CoChR (E103A), respectively containing single mutations homologous to the key mutations in ChETA_T and ChETA_A, achieved off-kinetics five times as fast as the off-kinetics of native CoChR ($p < 10^{-8}$ and 10^{-7} for E103T and E103A, respectively; two-sided Wilcoxon rank-sum test; $n = 23, 18,$ and 26 cells for E103T, E103A, and native CoChR, respectively) (Fig. 2 *b*; materials and methods). Their normalized peak and steady-state photocurrent amplitudes were significantly less than the peak and steady-state amplitudes of native CoChR, respectively ($p < 10^{-2}$ and 10^{-3} for E103T and E103A peak photocurrent, respectively; $p < 10^{-3}$ and 10^{-2} for E103T and E103A steady-state photocurrent, respectively; two-sided Wilcoxon rank-sum test; $n = 11, 18,$ and 15 cells for E103T, E103A, and native CoChR, respectively) (Fig. 2 *c*; materials and methods). On the other hand, the CoChR (T139C) or CoChR (L112C), which contained single mutations homologous to the key mutations in ChR2-TC and CatCh, respectively, exhibited significantly slower off-kinetics than the kinetics of native CoChR ($p < 10^{-7}$ and 10^{-10} for T139C and L112C, respectively; two-sided Wilcoxon rank-sum test; $n = 21, 41,$ and 26 cells for T139C, L112C, and native CoChR, respectively) (Fig. 2 *b*), and also significantly higher peak and steady-state photocurrent amplitude ($p < 0.05$ and 10^{-3} for T139C and L112C peak photocurrent, respectively; $p < 0.05$ and 10^{-5} for T139C and L112C steady-state photocurrent, respectively; two-sided Wilcoxon rank-sum test; $n = 20, 16,$ and 15 cells for T139C, L112C, and native CoChR, respectively) (Fig. 2 *c*). CoChR (H114R), containing the mutation homologous to the key mutation in ChR2_R, exhibited slightly faster off-kinetics ($p = 0.03$; two-sided Wilcoxon rank-sum test; $n = 24$ and 26 cells for H114R and native CoChR, respectively) (Fig. 2 *b*) but no significant improvement in either peak or steady-state photocurrent amplitude ($p = 0.65$ and 0.35 for peak and steady-state photocurrent, respectively; two-sided Wilcoxon rank-sum test; $n = 14$ and 15 cells for H114R and native CoChR, respectively) (Fig. 2 *c*). CoChR (H94E), which was previously reported to enhance the photosensitivity of CoChR (37,43), had a photocurrent amplitude twice that of native

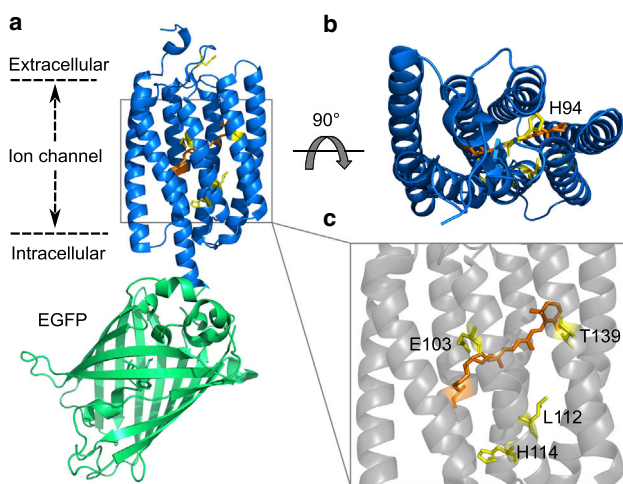


FIGURE 1 Targeted mutations around the ion pore and retinal Schiff base enhanced channel kinetics and ion conductivity of CoChR. (*a*) Side view, (*b*) top view, and (*c*) zoomed-in view of CoChR-EGFP. Also shown are the protonated RSB (orange) and key residues (yellow) that alter ion transport activity in stick form.

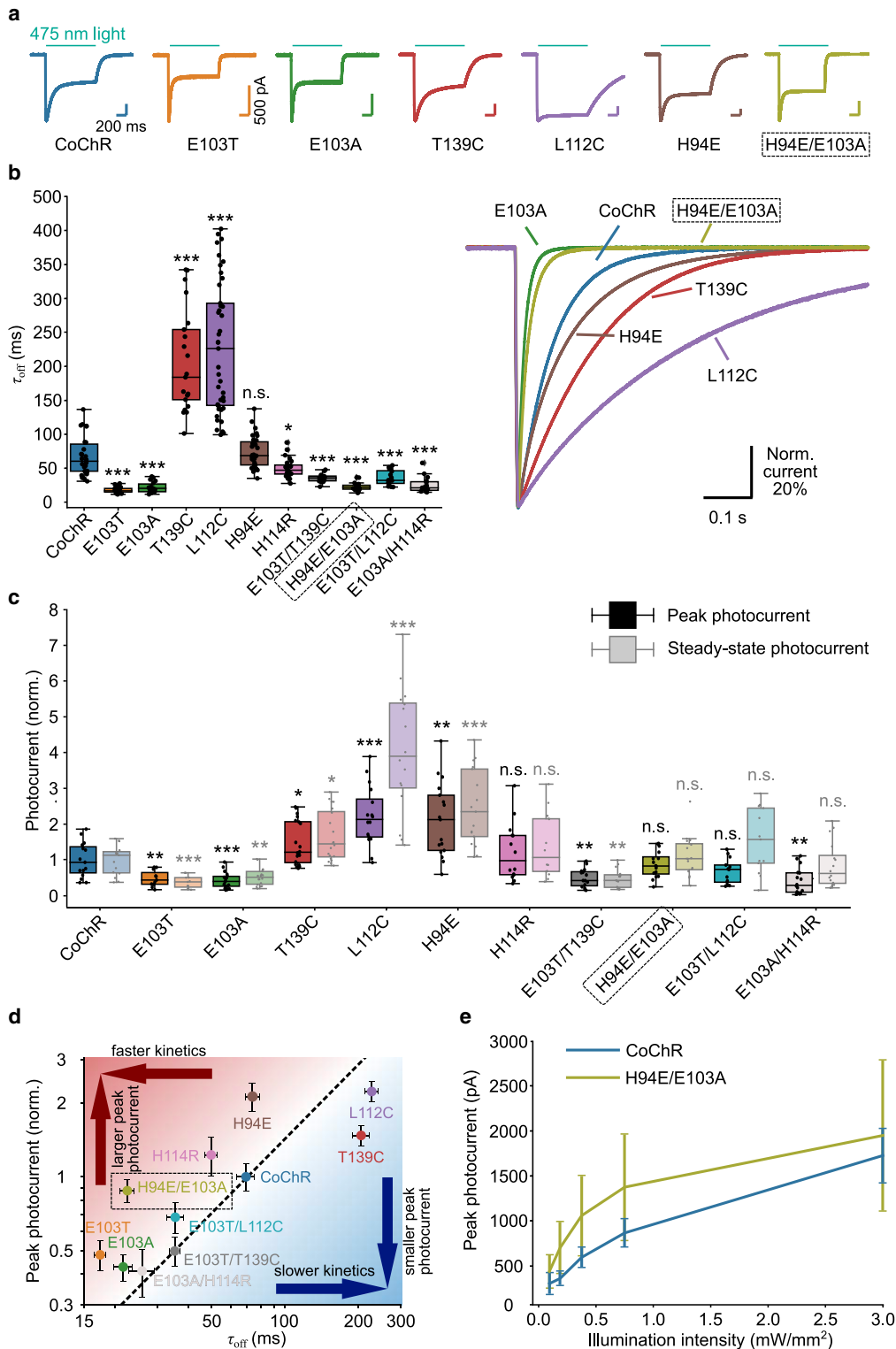


FIGURE 2 CoChR variants expressed in HEK293T cells exhibited different kinetic and photocurrent properties in response to cyan light stimulation at non-saturating excitation power densities. (a) Representative photocurrent traces of different CoChR variants elicited by 1 s cyan light illumination. (b, left) The τ_{off} and (c) the normalized peak and steady-state photocurrents (see materials and methods). We normalized the average photocurrent values of each CoChR variant such that the mean value for native CoChR was unity. Individual data points represent individual cells; boxplot displays outliers, the minimum value, the first quartile, the median value, the third quartile, and the maximum value; the vertical whisker extends to show the rest of distribution. Statistical tests compared metrics from each CoChR variant with the equivalent metric from native CoChR. n.s., not significant ($p > 0.05$); * $p < 0.05$, ** $p < 0.01$, *** $p < 0.001$. p -values were calculated with the two-sided Wilcoxon rank-sum test; $n > 10$ for all tested variants. (b, right) Representative normalized (legend continued on next page)

CoChR ($p < 10^{-2}$ and 10^{-4} for peak and steady-state photocurrent, respectively; two-sided Wilcoxon rank-sum test; $n = 17$ and 15 cells for H94E and native CoChR, respectively) (Fig. 2 *c*) while maintaining off-kinetics comparable to native CoChR ($p = 0.21$; two-sided Wilcoxon rank-sum test; $n = 31$ and 26 cells for H94E and native CoChR, respectively) (Fig. 2, *b* and *c*). We found an inverse relationship between peak photocurrent amplitude and off-kinetics (Fig. 2 *d*).

To circumvent this trade-off, we created four additional CoChR variants that combined mutations that accelerated off-kinetics with mutations that improved peak photocurrent (Figs. 2 *a* and S2 *a*). Among these CoChR variants, CoChR (H94E/E103A) had off-kinetics that were three times as fast as the off-kinetics of native CoChR ($p < 10^{-7}$; two-sided Wilcoxon rank-sum test; $n = 18$ and 26 cells for H94E/E103A and native CoChR, respectively) (Fig. 2, *a* and *b*) and had a similar peak photocurrent as that of native CoChR ($p = 0.62$ and 0.71 for peak and steady-state photocurrent, respectively; two-sided Wilcoxon rank-sum test; $n = 16$ and 15 cells for H94E/E103A and native CoChR, respectively; Figs. 2, *b–d* and S1). CoChR (H94E/E103A) demonstrated slightly higher orange light-driven peak photocurrent compared to native CoChR, especially at higher excitation intensities (Fig. S2 *b*). The reversal potential of CoChR (H94E/E103A) was 20 mV, which was 5 mV lower than the reversal potential of native CoChR (Fig. S2 *c*). The electrostatic potential of the CoChR ion pore surface (H94E/E103A) was more negative compared with that of native CoChR (Fig. S2, *d* and *e*; Table S1; materials and methods). We reasoned that this negative electrostatic potential might contribute to the increase in photocurrent amplitude. We anticipated that CoChR (H94E/E103A) possessed large photocurrent amplitude sufficient to depolarize neurons above their spike threshold because it generated large peak photocurrent (>500 pA) when stimulated with 5 ms light pulses at moderate power densities (Fig. 2 *e*).

To further evaluate the performance of CoChR (H94E/E103A), we directly compared CoChR (H94E/E103A) with other latest-generation opsins (11,30,44). In general, CoChR (H94E/E103A) was comparable with two state-of-art channelrhodopsins, Chronos (30) and CheRiff (11), in terms of photocurrent amplitude, channel kinetics, and the inevitable trade-off between them (Fig. S3, *a–d*). Additionally, CoChR (H94E/E103A) had larger photocurrent and faster kinetics than ChrimsonR (30), a red-shifted channelrhodopsin widely used in dual-channel experiments (Fig. S3, *a–c*). As one of the most potent optogenetic actuators, ChroME demonstrated both significantly larger photocurrent amplitude and moderate channel kinetics when

compared with CoChR (H94E/E103A) (Fig. S3, *a–d*) (44,45). Although ChroME had large peak photocurrent, it was more susceptible to crosstalk in dual-channel experiments in two ways (Fig. S3, *e–g*). First, ChroME was more susceptible to photocurrent when illuminated by only orange light used for red-fluorescence imaging: the average net photocurrent elicited by orange light at 0.5 mW/mm² was about 60 pA in ChroME-expressing HEK293T cells (Fig. S3 *f*). Such photocurrent was 10 times greater than the photocurrent elicited in CoChR (H94E/E103A) under the same conditions. Such photocurrent would depolarize neurons and prevent temporally precise control of neurons in dual-channel experiments when the orange imaging light was constantly on. Second, ChroME's photocurrent was suppressed under simultaneous orange and cyan illumination (Fig. S3, *e* and *g*). Although CoChR (H94E/E103A) had less photosensitivity than ChroME, its cyan light-driven photocurrent was less suppressed by constant orange light illumination because of its more blue-shifted action spectrum (Figs. S2 *b* and S3, *e–g*). Therefore, we anticipated that CoChR (H94E/E103A) would facilitate low-crosstalk, high-fidelity dual-channel experiments when combined with red-shifted indicators and complementary optical design.

The fast channel kinetics of CoChR (H94E/E103A) enhanced high-frequency spiking fidelity in cultured neurons

When expressed in cultured hippocampal pyramidal neurons, CoChR (H94E/E103A) possessed not only sufficient photosensitivity to depolarize the cell membrane at low illumination intensity but also off-kinetics fast enough to evoke high-frequency spikes with high fidelity (Figs. 3 and S4). CoChR (H94E/E103A) had off-kinetics faster than that of native CoChR when expressed in cultured neurons (Fig. S4 *a*). We stimulated cultured neurons expressing either native CoChR or CoChR (H94E/E103A) with a range of light pulse frequencies and illumination intensities. The spiking probability of neurons expressing both variants decreased with increasing stimulation frequency (Figs. 3, *a* and *b* and S4, *b* and *d*). However, CoChR (H94E/E103A) could accurately drive trains of single action potentials at stimulation frequencies higher than that of native CoChR: CoChR (H94E/E103A) reached a 50% spiking probability at 25 Hz stimulation, while native CoChR reached a 50% spiking probability at 17 Hz ($p < 10^{-3}$ at 1 mW/mm² and 3 mW/mm²; two-sided Wilcoxon rank-sum test; $n = 8$ and 10 cells for CoChR (H94E/E103A) and native CoChR at 1 mW/mm²; $n = 9$ cells for CoChR

photocurrent decay traces from different variants elicited by 5 ms cyan light pulses. (*d*) The τ_{off} versus normalized peak photocurrents demonstrates the trade-off between kinetics and photocurrent amplitude. Error bars represent SEM; the dashed line represents a performance isocontour of native CoChR. Illumination intensity was 1 mW/mm² for (*a–d*). (*e*) Peak photocurrent amplitude across a range of illumination intensities. Error bars represent SEM. $n = 5$ and 9 cells for CoChR (H94E/E103A) and native CoChR, respectively.

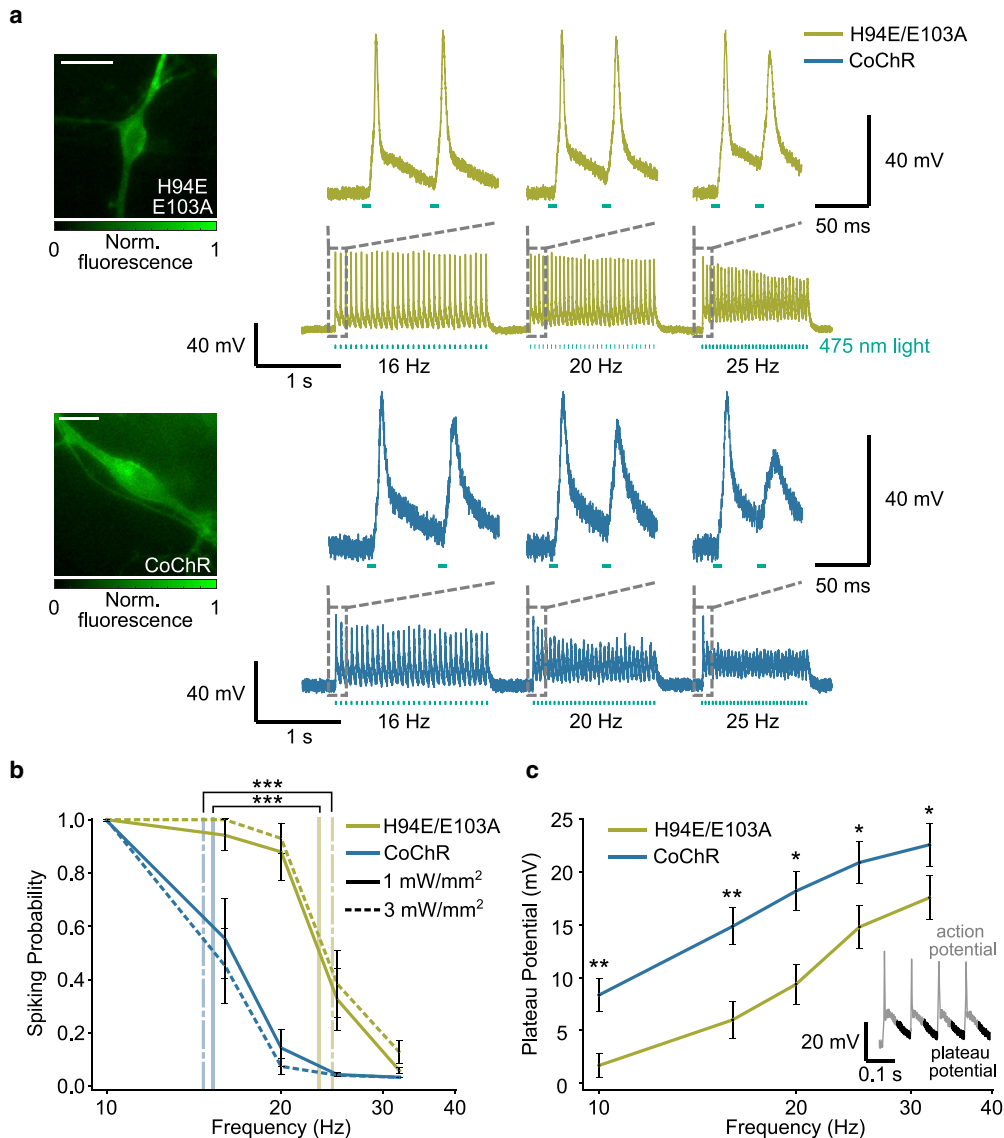


FIGURE 3 The fast channel kinetics of CoChR (H94E/E103A) enhanced high-frequency spiking fidelity in cultured neurons. (a) Left: fluorescence images of cultured hippocampal pyramidal neurons expressing CoChR (H94E/E103A) or native CoChR tagged with EGFP. Scale bar, 20 μm . Right: representative cyan light-driven spiking traces at the indicated frequencies at 1 mW/mm². Top insets: zoomed-in view of the first two spikes for each indicated stimulation frequency. (b) Average cyan light excitation-driven spiking probability at 1 mW/mm² (solid line) and 3 mW/mm² (dashed line) illumination intensities decreased with increasing frequency. Vertical lines show the average stimulation frequencies for 50% spiking probability for each construct and excitation power. The average stimulation frequencies for 50% spiking probability for CoChR (H94E/E103A)-expressing neurons at 1 mW/mm² (vertical yellow solid line) and at 3 mW/mm² (vertical yellow dashed line) were significantly higher than the respective values of native CoChR-expressing neurons (blue solid line at 1 mW/mm²; blue dashed line at 3 mW/mm²). Error bars represent SEM; *** $p < 10^{-3}$. p -values were calculated with two-sided Wilcoxon rank-sum test; $n = 8$ and 10 cells for CoChR (H94E/E103A) and native CoChR at 1 mW/mm²; $n = 9$ cells for CoChR (H94E/E103A) and native CoChR at 3 mW/mm². All cyan light spiking protocols used a train of 30 pulses (5 ms width) ranging from 10 Hz to 32 Hz at 1 mW/mm² and 3 mW/mm². (c) Plateau potentials induced by cyan light pulse trains elevated with increasing frequency. Inset: voltage recording (gray) and plateau potential components (black) from one example trace containing light-driven spikes. Error bars represent SEM; * $p < 0.05$, ** $p < 0.01$. p -values were calculated with the two-sided Wilcoxon rank-sum test; $n = 8$ neurons.

(H94E/E103A) and native CoChR at 3 mW/mm²) (Figs. 3, a and b and S4 d; materials and methods). The decreases in spiking probability at high frequencies was likely due to depolarization block predominantly impacting the slow channelrhodopsin: the slower off-kinetics of native CoChR generated a higher plateau potential than the plateau poten-

tial of CoChR (H94E/E103A) at all stimulation frequencies ($p < 0.05$ at all stimulation frequencies; two-sided Wilcoxon rank-sum test; $n = 8$ cells) (Fig. 3 c; materials and methods). In addition, spike failures occurred later in the pulse trains for both native CoChR and CoChR (H94E/E103A), probably due to photocurrent desensitization over

the course of tens of pulses delivered close in time (Figs. 3 *a* and S4, *c* and *d*).

CoChR (H94E/E103A) enabled low-crosstalk dual-channel experiments with concurrent red-fluorescence calcium imaging

CoChR (H94E/E103A) facilitated simultaneous high-frequency optogenetic stimulation and calcium imaging with minimal photocurrent crosstalk (Fig. 4). To demonstrate the lack of spectral crosstalk, we photostimulated cultured hippocampal pyramidal neurons coexpressing CoChR (H94E/E103A) and jRCaMP1b with both 475 nm cyan light and 585 nm orange light (Fig. 4, *a* and *b*; materials and methods). The 475 nm cyan light pulses generated peak photocurrent sufficient to depolarize the neuron above its threshold (8 out of 12 neurons had greater than 500 pA), while 585 nm orange light pulses generated negligible photocurrent (11 out of 12 neurons had less than 20 pA) ($p < 10^{-4}$ for comparison using cyan light- and orange light-driven photocurrent; two-sided Wilcoxon rank-sum test; $n = 12$ cells) (Fig. 4 *b*). We next demonstrated the application of CoChR (H94E/E103A) in low-crosstalk dual-channel experiments with concurrent red-fluorescence

calcium imaging. We simultaneously applied three 5 ms, 475 nm light pulses at 40 ms intervals, recorded the neuron's electrophysiology by whole-cell patch clamp, and recorded the fluorescence change ($\Delta F/F$) of jRCaMP1b (Fig. 4 *c*; materials and methods). The whole-cell electrophysiology confirmed the light-induced action potentials matched to the fluorescence transients within the fluorescence traces. The peak red-fluorescence response was even larger in unpatched neurons, because calcium influx from the patch pipette intracellular solution did not impact intracellular Ca^{2+} concentration (Fig. S5 *a*). We ruled out the possibility of photoswitching-induced fluorescence transients by photostimulating neurons expressing only jRCaMP1b. Because 475 nm photostimulation of these neurons did not induce transient fluorescence (Fig. 4 *d*), we confirmed that the fluorescence transients in rhodopsin-expressing neurons were due to calcium ion influx following light-induced action potentials.

The combination of blue-shifted CoChR (H94E/E103A) with red-shifted jRCaMP1b had less photocurrent crosstalk than the combination of red-shifted ChrimsonR with green calcium indicators such as GCaMP6 in one-photon dual-channel experiments. To directly compare the applications of these two different actuator-indicator pairs in one-photon

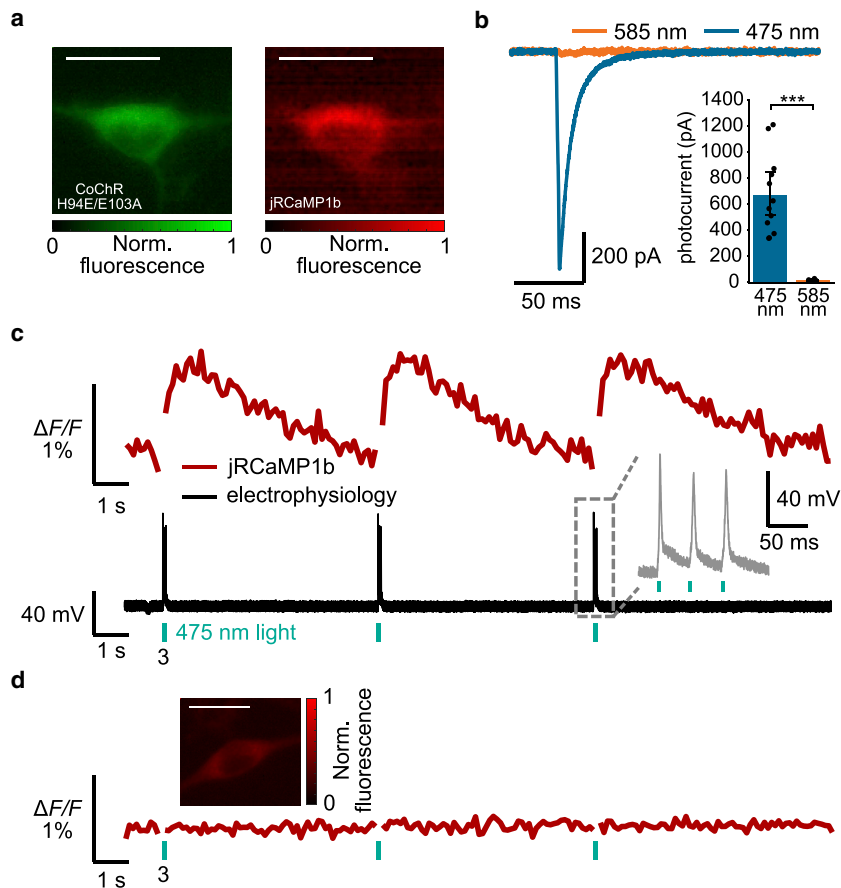


FIGURE 4 CoChR (H94E/E103A) enabled low-crosstalk dual-channel experiments with concurrent red-fluorescence calcium imaging in cultured neurons. (a) Cultured hippocampal pyramidal neuron coexpressed CoChR (H94E/E103A) tagged with EGFP (left) and jRCaMP1b (right). Scale bar, 20 μm . (b) The 475 nm excitation produced ample depolarization photocurrent, while the 585 nm excitation generated minimal photocurrent. Inset: summary plots of photocurrent elicited by 475 nm and 585 nm light pulses. Data points represent individual cells. Error bars represent SEM; *** $p < 0.001$; two-sided Wilcoxon rank-sum test; $n = 12$ neurons. (c) Cyan light pulses induced changes in fluorescence in cultured hippocampal pyramidal neurons expressing CoChR (H94E/E103A) and jRCaMP1b. Simultaneous calcium (top) and electrophysiology (bottom) recordings via jRCaMP1b and whole-cell current clamp, respectively, confirmed that changes in jRCaMP1b fluorescence were induced by action potentials. The cyan light pulse protocol used a train of three pulses (5 ms width) at 1 mW/mm^2 at 25 Hz followed by a 6 s interval. Light pulses were limited within single frames. Fluorescence signals corresponding to frames with photostimulation artifacts were removed. Insets: zoomed-in view of the cyan light excitation-driven action potentials. (d) Cultured pyramidal neuron only expressing jRCaMP1b did not exhibit significant cyan light excitation-driven photoswitching. Inset: fluorescence image of cultured pyramidal neuron expressing only jRCaMP1b. Scale bars, 20 μm .

dual-channel experiments, we first photostimulated cultured hippocampal pyramidal neurons expressing ChrimsonR with 585 nm orange light pulses (Fig. S5, *b* and *c*; [materials and methods](#)). We then applied constant 475 nm cyan light illumination simulating the imaging of GCaMP6 and photostimulated the neurons using orange light pulses (Fig. S5, *b* and *c*; [materials and methods](#)). Orange light pulses successfully elicited spikes in cultured hippocampal pyramidal neurons expressing ChrimsonR without constant cyan light illumination but failed to elicit spikes with constant cyan light illumination (Fig. S5 *b*). Such spike failure was possibly due to the dampened orange light-driven photocurrent amplitude caused by a faster channel closure rate under constant cyan light illumination (46–48) (Fig. S5, *c* and *d*).

DISCUSSION

In this work, we demonstrated a kinetic-optimized CoChR (H94E/E103A) variant that extended the frequency range for stimulating spikes in cultured neurons with high fidelity and supported one-photon dual-channel optogenetic applications. Two advancements of CoChR (H94E/E103A) were the faster off-kinetics compared with kinetics of native CoChR, and minimal photoactivation crosstalk during simultaneous stimulation and fluorescence imaging with a red calcium indicator.

Our rational optimization improved CoChR by combining two single-amino-acid substitutions respectively governing electronic interaction with the RSB and the channel ion transport. The E103A mutation destabilized an RSB counterion and accelerated the channel kinetics, but reduced the photocurrent amplitude (31). The H94E mutation then successfully circumvented this photocurrent reduction. Because H94 was on the extracellular loop between transmembrane helix 2 and helix 3, we proposed a potential mechanism for how H94E increased photocurrent based on our simulation: the negatively charged H94E could enhance the electrostatic interaction between the ion pore entrance formed by helices 1, 2, 3, and 7 (33) and cations in the extracellular space. In the future, a detailed investigation of the H94E mutation could further elucidate the underlying mechanism of its resulting photocurrent enhancement.

Our results demonstrated that the accelerated channel kinetics of CoChR (H94E/E103A) enhanced spiking fidelity in cultured neurons. Different channel off-rates are favored depending on different experimental settings. For example, faster channelrhodopsins are standard optogenetic tools for precise optical control of neuron populations in combination with one-photon illumination techniques. Some recently developed channelrhodopsins have fast kinetics (30,31,36,44,49), which enabled improved temporal precision and spiking fidelity that were especially useful for neuroscientific research involving fast-spiking systems (50) or the induction of synaptic plasticity (51). For example, the ultrafast kinetics of Chronos enabled sub-millisecond control of high-frequency firing in inhibitory interneurons; high-frequency

light stimulation of ChETA-expressing terminals in the medial prefrontal cortex induced long-term potentiation (34,35). CoChR (H94E/E103A) is still slower than fast channelrhodopsins such as Chronos, but still elicits spike trains up to 25 Hz in cultured hippocampal neurons, which is sufficient for most neuroscience studies involving sparsely firing systems (52). Because the basic biophysical and photocurrent properties of channelrhodopsins are consistent regardless of neuron preparation, multiple previous studies successfully translated applications from neuron cultures into acute brain slices or live mammalian models (30,36). Therefore, we reasoned that our demonstration of the dual-channel experiment would likely be translatable to acute brain slices or live mammalian models as well. It is likely that our CoChR variant can drive even greater spike rates in live mammalian models at higher body temperature and in fast-spiking cell types (9,36,53,54).

On the other hand, moderate channel off-kinetics of tens to hundreds of milliseconds could be beneficial in some applications. In one example, CoChR-LC and CoChR-3M demonstrated prolonged off-kinetics and enhanced photocurrent when expressed in retinal ganglion cells (43). In addition, rapid repolarization due to fast off-kinetics becomes unfavorable for two-photon optogenetics. While two-photon excitation confines the excitation volume in the axial direction and provides sectioning capabilities in scattering tissue, the femtoliter two-photon excitation volume also limits the number of simultaneously activated channelrhodopsins. Thus, two-photon excitation disfavors fast channelrhodopsins that do not integrate sufficient photocurrent to depolarize the neuron above its threshold (21,55), and instead favors channelrhodopsins with kinetics that match the duration of the scanning illumination (35,55). Our CoChR variant's 15–30 ms off time is in the range of two-photon photostimulation scan times. Two-photon holographic illumination of interneurons expressing native CoChR already generated light-driven action potential trains up to 100 Hz (56). Our CoChR (H94E/E103A) variant's superior kinetics compared with native CoChR could further increase temporal precision when driving high-frequency spike trains by decreasing the plateau potential.

Our CoChR (H94E/E103A) had a blue-shifted excitation spectrum that enabled low-crosstalk dual-channel experiments when paired with red-shifted optogenetic actuators or genetically encoded indicators. The simultaneous use of two spectrally separated actuators allows independent optical stimulation of distinct neural populations. For example, the combination of Chronos and Chrimson enabled two-color activation of neural spiking and downstream synaptic transmission in distinct neural populations without detectable crosstalk (30). However, spectral crosstalk in such dual-channel optogenetic experiments always occurs because of the long blue tail of the rhodopsin absorption spectrum. Such crosstalk could hinder simultaneous manipulation of two distinct neuron populations or limit complete independent

activation to a narrow range of intensities for blue-light excitation. Our CoChR (H94E/E103A) is more blue-shifted than Chronos and has channel kinetics similar to that of Chrimson. Therefore, when paired with Chrimson, CoChR (H94E/E103A) may enable low-crosstalk two-color *in vivo* activation within a larger window of blue-light illumination powers.

In experiments using simultaneous optogenetic stimulation and imaging, spectral crosstalk becomes a problem when imaging light directly activates optogenetic actuators and causes unwanted neural perturbation. Modern engineering has been addressing this by expanding the spectral diversity of both genetically encoded actuators and indicators (24,30,36,57–61). This multicolor suite of protein tools has given rise to more spectrally separated actuator-indicator pairs that could minimize photocurrent crosstalk. Our CoChR (H94E/E103A) was compatible with red-shifted genetically encoded calcium indicators, such as jRCaMP1b, in one-photon dual-channel experiments that had minimal undesirable neuron activation by imaging light. Of the red-fluorescent calcium indicators, we used jRCaMP1b for its minimal photoswitching under simultaneous cyan light illumination (24). On the other hand, we showed that a combination of the green genetically encoded calcium indicator GCaMP6 and the red-shifted channelrhodopsin ChrimsonR would not be able to simultaneously manipulate and record the neural activity, due to non-negligible photocurrent crosstalk. Our dual-channel experiment employing simultaneous optogenetic stimulation and imaging not only took advantage of our CoChR variant's blue-shifted absorption, but also relied on an optical design that further avoided the spectral overlap between imaging light and the CoChR absorption spectrum. The excitation light wavelength (475 nm) stimulated the peak of CoChR absorption spectrum while the imaging light wavelength (585 nm) minimally overlapped with the CoChR absorption spectrum (26,62). In our previous work, we engineered a red genetically encoded voltage indicator, Ace-mScarlet (60), which required high illumination power in the red imaging channel. However, Ace-mScarlet's high signal-to-noise ratio in cultured settings could allow the use of moderate imaging powers of 1 mW/mm² that could avoid inadvertent depolarization of CoChR (H94E/E103A)-expressing neurons. Ongoing protein engineering of fluorescent indicators could further extend the spectral separation and reduce the need for custom optical design. For example, deep-red and NIR calcium indicators, such as R-GECO1 (29), CaSiR-1 (63), iGECI (27), and NIR-GECO1 (26), enabled minimal crosstalk or even crosstalk-free compatibility with blue- or green-light-activated actuators such as CheRiff (11,64,65), ChR2 (4), and Chronos (30,66). We anticipate that, in combination with these calcium indicators and complementary optical design, our CoChR (H94E/E103A) would demonstrate similar or even better performance than that of some existing blue-shifted actuators, thanks to its larger peak photocurrent amplitude and moderate channel kinetics.

Although the pairing of CoChR (H94E/E103A) and jRCaMP1b minimized the possibility for photocurrent crosstalk from the excitation of the indicator, the pair did not eliminate fluorescence crosstalk artifacts due to jRCaMP1b's non-negligible absorption at cyan wavelengths. We observed these transient increases in the fluorescence of the red imaging channel during cyan light stimulation of CoChR (H94E/E103A). To address this fluorescence crosstalk caused by direct excitation of jRCaMP1b by cyan light, we limited cyan excitation light pulses to single imaging frames. We then removed frames containing fluorescence crosstalk artifacts. Because the rise time of jRCaMP1b fluorescence was longer than one frame (100 ms), our method maintained the fidelity of calcium transients evoked by cyan light-driven action potentials. A generalizable, blind algorithm could further automatically predict the occurrence of fluorescence artifacts and remove artifacts by subtracting a predicted template waveform (60).

Our optimization of CoChR followed a rational optimization pipeline widely used in modern protein engineering. Such rational engineering strategies use established knowledge of protein structure to create chimeras or graft known mutations onto homologous sequences (67,68). Rational optimization has been an effective way to generate novel optogenetic actuators with improved functional properties (21,38,43,58,69), but the rational engineering pipeline is relatively low throughput. Additionally, the scalability and applicability of rational design are often limited by the homology between variants. For example, in our CoChR variant, the E103 residue is conserved among many other channelrhodopsins, governing the channel-open duration (30,70,71). Therefore, we hypothesize that mutations homologous to E103A may cause similar effects in other channelrhodopsins. However, unlike the E103 residue, the H94 residue is not conserved among channelrhodopsins (30,37,43). Therefore, we suspect that the H94E mutation would not be as broadly applicable as E103A mutation. Recent application of large-scale pipelines, such as transcriptome sequencing, high-throughput library screening, and machine-learning-guided functionality prediction, has partially addressed these limitations (30,72,73). In the future, a combination of rationally designed mutations and large-scale screens could continue the optimization of more blue-shifted channelrhodopsins, such as TsChR (30) and KnChR (23); such rhodopsins could further separate the opsin excitation wavelength from the imaging wavelength in dual-channel experiments.

CONCLUSION

We described CoChR (H94E/E103A), a kinetic-optimized CoChR variant. CoChR (H94E/E103A) had an off time that was one-third that of native CoChR, and minimal fluorescence crosstalk when used simultaneously with a red calcium indicator. The additive effect of two amino acid

substitutions accounted for our variant's enhanced photocurrent and channel kinetics. One mutation (H94E) enhanced the photocurrent amplitude by altering ion transport, while the other mutation (E103A) accelerated the channel kinetics by destabilizing an RSB counterion. In cultured neurons, our CoChR variant drove action potentials with high fidelity at frequencies higher than those reached by native CoChR. Our CoChR variant's blue-shifted excitation spectrum enabled low-crosstalk dual-channel experiments with concurrent red-fluorescence calcium imaging. The large photocurrent amplitude and moderate channel kinetics of our CoChR variant could have additional applications in two-photon optogenetics that integrate photocurrent over millisecond-duration scans.

SUPPORTING MATERIAL

Supporting material can be found online at <https://doi.org/10.1016/j.bpj.2022.09.024>.

AUTHOR CONTRIBUTIONS

X.B. and Y.G. conceived and designed all experiments. X.B. and C.B. performed the experiments and analyzed the data. Y.G. supervised the research. X.B., C.B., and Y.G. wrote the manuscript. All authors edited the manuscript.

ACKNOWLEDGMENTS

We thank funding from the NIH New Innovator Program (IDP2-NS111505), the Arnold and Mabel Beckman Foundation, and the Vallee Foundation.

DECLARATION OF INTERESTS

The authors declare no competing interests.

REFERENCES

1. Yizhar, O., L. E. Fenno, ..., K. Deisseroth. 2011. Optogenetics in neural systems. *Neuron*. 71:9–34. <https://doi.org/10.1016/j.neuron.2011.06.004>.
2. Tye, K. M., and K. Deisseroth. 2012. Optogenetic investigation of neural circuits underlying brain disease in animal models. *Nat. Rev. Neurosci.* 13:251–266. <https://doi.org/10.1038/nrn3171>.
3. Kim, C. K., A. Adhikari, and K. Deisseroth. 2017. Integration of optogenetics with complementary methodologies in systems neuroscience. *Nat. Rev. Neurosci.* 18:222–235. <https://doi.org/10.1038/nrn.2017.15>.
4. Nagel, G., T. Szellas, ..., E. Bamberg. 2003. Channelrhodopsin-2, a directly light-gated cation-selective membrane channel. *Proc. Natl. Acad. Sci. USA*. 100:13940–13945. <https://doi.org/10.1073/pnas.1936192100>.
5. Zhao, S., J. T. Ting, ..., G. Feng. 2011. Cell type-specific channelrhodopsin-2 transgenic mice for optogenetic dissection of neural circuitry function. *Nat. Methods*. 8:745–752. <https://doi.org/10.1038/nmeth.1668>.
6. Allen, W. E., M. Z. Chen, ..., K. Deisseroth. 2019. Thirst regulates motivated behavior through modulation of brainwide neural population dynamics. *Science*. 364:253. <https://doi.org/10.1126/science.aav3932>.
7. Spix, T. A., S. Nanivadekar, ..., A. H. Gittis. 2021. Population-specific neuromodulation prolongs therapeutic benefits of deep brain stimulation. *Science*. 374:201–206. <https://doi.org/10.1126/science.abi7852>.
8. Petreanu, L., D. Huber, ..., K. Svoboda. 2007. Channelrhodopsin-2-assisted circuit mapping of long-range callosal projections. *Nat. Neurosci.* 10:663–668. <https://doi.org/10.1038/nn1891>.
9. Arenkiel, B. R., J. Peca, ..., G. Feng. 2007. In vivo light-induced activation of neural circuitry in transgenic mice expressing channelrhodopsin-2. *Neuron*. 54:205–218. <https://doi.org/10.1016/j.neuron.2007.03.005>.
10. Akerboom, J., N. Carreras Calderón, ..., L. L. Looger. 2013. Genetically encoded calcium indicators for multi-color neural activity imaging and combination with optogenetics. *Front. Mol. Neurosci.* 6:2. <https://doi.org/10.3389/fnmol.2013.00002>.
11. Hochbaum, D. R., Y. Zhao, ..., A. E. Cohen. 2014. All-optical electrophysiology in mammalian neurons using engineered microbial rhodopsins. *Nat. Methods*. 11:825–833. <https://doi.org/10.1038/nmeth.3000>.
12. Yang, W., L. Carrillo-Reid, ..., R. Yuste. 2018. Simultaneous two-photon imaging and two-photon optogenetics of cortical circuits in three dimensions. *Elife*. 7:e32671. <https://doi.org/10.7554/eLife.32671>.
13. Daie, K., K. Svoboda, and S. Druckmann. 2021. Targeted photostimulation uncovers circuit motifs supporting short-term memory. *Nat. Neurosci.* 24:259–265. <https://doi.org/10.1038/s41593-020-00776-3>.
14. Jennings, J. H., C. K. Kim, ..., K. Deisseroth. 2019. Interacting neural ensembles in orbitofrontal cortex for social and feeding behaviour. *Nature*. 565:645–649. <https://doi.org/10.1038/s41586-018-0866-8>.
15. Fan, L. Z., S. Kheifets, ..., A. E. Cohen. 2020. All-optical electrophysiology reveals the role of lateral inhibition in sensory processing in cortical layer 1. *Cell*. 180:521–535.e18. <https://doi.org/10.1016/j.cell.2020.01.001>.
16. Yizhar, O., L. E. Fenno, ..., K. Deisseroth. 2011. Neocortical excitation/inhibition balance in information processing and social dysfunction. *Nature*. 477:171–178. <https://doi.org/10.1038/nature10360>.
17. Rajasethupathy, P., S. Sankaran, ..., K. Deisseroth. 2015. Projections from neocortex mediate top-down control of memory retrieval. *Nature*. 526:653–659. <https://doi.org/10.1038/nature15389>.
18. Wilson, N. R., C. A. Runyan, ..., M. Sur. 2012. Division and subtraction by distinct cortical inhibitory networks in vivo. *Nature*. 488:343–348. <https://doi.org/10.1038/nature11347>.
19. Zhang, Y. P., and T. G. Oertner. 2007. Optical induction of synaptic plasticity using a light-sensitive channel. *Nat. Methods*. 4:139–141. <https://doi.org/10.1038/nmeth988>.
20. Chen, T. W., T. J. Wardill, ..., D. S. Kim. 2013. Ultrasensitive fluorescent proteins for imaging neuronal activity. *Nature*. 499:295–300. <https://doi.org/10.1038/nature12354>.
21. Prakash, R., O. Yizhar, ..., K. Deisseroth. 2012. Two-photon optogenetic toolbox for fast inhibition, excitation and bistable modulation. *Nat. Methods*. 9:1171–1179. <https://doi.org/10.1038/nmeth.2215>.
22. Packer, A. M., L. E. Russell, ..., M. Häusser. 2015. Simultaneous all-optical manipulation and recording of neural circuit activity with cellular resolution in vivo. *Nat. Methods*. 12:140–146. <https://doi.org/10.1038/nmeth.3217>.
23. Tashiro, R., K. Sushmita, and S. P. Tsunoda. 2021. Specific residues in the cytoplasmic domain modulate photocurrent kinetics of channelrhodopsin from *Klebsormidium nitens*. *Commun. Biol.* 4:235. <https://doi.org/10.1038/s42003-021-01755-5>.
24. Dana, H., B. Mohar, ..., D. S. Kim. 2016. Sensitive red protein calcium indicators for imaging neural activity. *Elife*. 5:e12727. <https://doi.org/10.7554/eLife.12727>.
25. Kannan, M., G. Vasan, ..., V. A. Pieribone. 2018. Fast, in vivo voltage imaging using a red fluorescent indicator. *Nat. Methods*. 15:1108–1116. <https://doi.org/10.1038/s41592-018-0188-7>.

26. Qian, Y., K. D. Piatkevich, ..., R. E. Campbell. 2019. A genetically encoded near-infrared fluorescent calcium ion indicator. *Nat. Methods*. 16:171–174. <https://doi.org/10.1038/s41592-018-0294-6>.
27. Shemetov, A. A., M. V. Monakhov, ..., V. V. Verkhusha. 2021. A near-infrared genetically encoded calcium indicator for in vivo imaging. *Nat. Biotechnol.* 39:368–377. <https://doi.org/10.1038/s41587-020-0710-1>.
28. Deo, C., A. S. Abdelfattah, ..., E. R. Schreier. 2021. The HaloTag as a general scaffold for far-red tunable chemigenetic indicators. *Nat. Chem. Biol.* 17:718–723. <https://doi.org/10.1038/s41589-021-00775-w>.
29. Zhao, Y., S. Araki, ..., R. E. Campbell. 2011. An expanded palette of genetically encoded Ca²⁺ indicators. *Science*. 333:1888–1891. <https://doi.org/10.1126/science.1208592>.
30. Klapoetke, N. C., Y. Murata, ..., E. S. Boyden. 2014. Independent optical excitation of distinct neural populations. *Nat. Methods*. 11:338–346. <https://doi.org/10.1038/nmeth.2836>.
31. Gunaydin, L. A., O. Yizhar, ..., P. Hegemann. 2010. Ultrafast optogenetic control. *Nat. Neurosci.* 13:387–392. <https://doi.org/10.1038/nn.2495>.
32. Berndt, A., P. Schoenenberger, and T. G. Oertner. 2011. High-efficiency channelrhodopsins for fast neuronal stimulation at low light levels. *Proc. Natl. Acad. Sci. USA*. 108:7595–7600. <https://doi.org/10.1073/pnas.1017210108>.
33. Deisseroth, K., and P. Hegemann. 2017. The form and function of channelrhodopsin. *Science*. 357:eaan5544. <https://doi.org/10.1126/science.aan5544>.
34. Bulin, S. E., K. M. Hohl, ..., D. A. Morilak. 2020. Bidirectional optogenetically-induced plasticity of evoked responses in the rat medial prefrontal cortex can impair or enhance cognitive set-shifting. *eNeuro*. 7. ENEURO.0363. <https://doi.org/10.1523/eneuro.0363-19.2019>.
35. Ronzitti, E., R. Conti, ..., V. Emiliani. 2017. Submillisecond optogenetic control of neuronal firing with two-photon holographic photoactivation of Chronos. *J. Neurosci.* 37:10679–10689. <https://doi.org/10.1523/jneurosci.1246-17.2017>.
36. Mattis, J., K. M. Tye, ..., K. Deisseroth. 2011. Principles for applying optogenetic tools derived from direct comparative analysis of microbial opsins. *Nat. Methods*. 9:159–172. <https://doi.org/10.1038/nmeth.1808>.
37. Doi, S., T. Tsukamoto, ..., Y. Sudo. 2017. An inhibitory role of Arg-84 in anion channelrhodopsin-2 expressed in *Escherichia coli*. *Sci. Rep.* 7:41879. <https://doi.org/10.1038/srep41879>.
38. Gong, X., D. Mendoza-Halliday, ..., G. Feng. 2020. An ultra-sensitive step-function opsin for minimally invasive optogenetic stimulation in mice and macaques. *Neuron*. 107:38–51.e8. <https://doi.org/10.1016/j.neuron.2020.03.032>.
39. Jumper, J., R. Evans, ..., D. Hassabis. 2021. Highly accurate protein structure prediction with AlphaFold. *Nature*. 596:583–589. <https://doi.org/10.1038/s41586-021-03819-2>.
40. Dolinsky, T. J., P. Czodrowski, ..., N. A. Baker. 2007. PDB2PQR: expanding and upgrading automated preparation of biomolecular structures for molecular simulations. *Nucleic Acids Res.* 35:W522–W525. <https://doi.org/10.1093/nar/gkm276>.
41. MacKerell, A. D., D. Bashford, ..., M. Karplus. 1998. All-atom empirical potential for molecular modeling and dynamics studies of proteins. *J. Phys. Chem. B*. 102:3586–3616. <https://doi.org/10.1021/jp973084f>.
42. Humphrey, W., A. Dalke, and K. Schulten. 1996. VMD: visual molecular dynamics. *J. Mol. Graph.* 14. 33-38:27-28, 27-38. [https://doi.org/10.1016/0263-7855\(96\)00018-5](https://doi.org/10.1016/0263-7855(96)00018-5).
43. Ganjawala, T. H., Q. Lu, ..., Z. H. Pan. 2019. Improved CoChR variants restore visual acuity and contrast sensitivity in a mouse model of blindness under ambient light conditions. *Mol. Ther.* 27:1195–1205. <https://doi.org/10.1016/j.ymthe.2019.04.002>.
44. Mardinly, A. R., I. A. Oldenburg, ..., H. Adesnik. 2018. Precise multimodal optical control of neural ensemble activity. *Nat. Neurosci.* 21:881–893. <https://doi.org/10.1038/s41593-018-0139-8>. <https://www.ncbi.nlm.nih.gov/pubmed/29713079>.
45. Sridharan, S., M. A. Gajowa, ..., H. Adesnik. 2022. High-performance microbial opsins for spatially and temporally precise perturbations of large neuronal networks. *Neuron*. 110:1139–1155.e6. <https://doi.org/10.1016/j.neuron.2022.01.008>.
46. Lin, J. Y. 2011. A user's guide to channelrhodopsin variants: features, limitations and future developments. *Exp. Physiol.* 96:19–25. <https://doi.org/10.1113/expphysiol.2009.051961>.
47. Stahlberg, M. A., C. Ramakrishnan, ..., C. Dean. 2019. Investigating the feasibility of channelrhodopsin variants for nanoscale optogenetics. *Neurophotonics*. 6:015007. <https://doi.org/10.1117/1.NPh.6.1.015007>.
48. Stehfest, K., E. Ritter, ..., P. Hegemann. 2010. The branched photocycle of the slow-cycling channelrhodopsin-2 mutant C128T. *J. Mol. Biol.* 398:690–702. <https://doi.org/10.1016/j.jmb.2010.03.031>.
49. Sridharan, S., M. Gajowa, ..., H. Adesnik. 2021. High performance microbial opsins for spatially and temporally precise perturbations of large neuronal networks. *Neuron*. 110:1139–1155.e6. <https://doi.org/10.1101/2021.04.01.438134>.
50. Cardin, J. A., M. Carlén, ..., C. I. Moore. 2009. Driving fast-spiking cells induces gamma rhythm and controls sensory responses. *Nature*. 459:663–667. <https://doi.org/10.1038/nature08002>.
51. Jackman, S. L., B. M. Beneduce, ..., W. G. Regehr. 2014. Achieving high-frequency optical control of synaptic transmission. *J. Neurosci.* 34:7704–7714. <https://doi.org/10.1523/jneurosci.4694-13.2014>.
52. Huber, D., L. Petreanu, ..., K. Svoboda. 2008. Sparse optical microstimulation in barrel cortex drives learned behaviour in freely moving mice. *Nature*. 451:61–64. <https://doi.org/10.1038/nature06445>.
53. Mager, T., D. Lopez de la Morena, ..., E. Bamberg. 2018. High frequency neural spiking and auditory signaling by ultrafast red-shifted optogenetics. *Nat. Commun.* 9:1750. <https://doi.org/10.1038/s41467-018-04146-3>.
54. Proskurina, E. Y., and A. V. Zaitsev. 2021. Photostimulation activates fast-spiking interneurons and pyramidal cells in the entorhinal cortex of Thy1-ChR2-YFP line 18 mice. *Biochem. Biophys. Res. Commun.* 580:87–92. <https://doi.org/10.1016/j.bbrc.2021.10.002>.
55. Adesnik, H., and L. Abdeladim. 2021. Probing neural codes with two-photon holographic optogenetics. *Nat. Neurosci.* 24:1356–1366. <https://doi.org/10.1038/s41593-021-00902-9>.
56. Papagiakoumou, E., E. Ronzitti, ..., V. Emiliani. 2018. Two-photon optogenetics by computer-generated holography. In *Neuromethods Series: Optogenetics: A Roadmap*. Springer, pp. 175–197. https://doi.org/10.1007/978-1-4939-7417-7_10.
57. Bi, X., C. Beck, and Y. Gong. 2021. Genetically encoded fluorescent indicators for imaging brain chemistry. *Biosensors*. 11:116. <https://doi.org/10.3390/bios11040116>.
58. Lin, J. Y., P. M. Knutsen, ..., R. Y. Tsien. 2013. ReaChR: a red-shifted variant of channelrhodopsin enables deep transcranial optogenetic excitation. *Nat. Neurosci.* 16:1499–1508. <https://doi.org/10.1038/nn.3502>.
59. Zhang, F., M. Prigge, ..., K. Deisseroth. 2008. Red-shifted optogenetic excitation: a tool for fast neural control derived from *Volvox carterii*. *Nat. Neurosci.* 11:631–633. <https://doi.org/10.1038/nn.2120>.
60. Beck, C., and Y. Gong. 2019. A high-speed, bright, red fluorescent voltage sensor to detect neural activity. *Sci. Rep.* 9:15878. <https://doi.org/10.1038/s41598-019-52370-8>.
61. Molina, R. S., Y. Qian, ..., T. E. Hughes. 2019. Understanding the fluorescence change in red genetically encoded calcium ion indicators. *Biophys. J.* 116:1873–1886. <https://doi.org/10.1016/j.bpj.2019.04.007>.
62. Shemesh, O. A., D. Tanese, ..., V. Emiliani. 2017. Temporally precise single-cell-resolution optogenetics. *Nat. Neurosci.* 20:1796–1806. <https://doi.org/10.1038/s41593-017-0018-8>.
63. Egawa, T., K. Hanaoka, ..., T. Nagano. 2011. Development of a far-red to near-infrared fluorescence probe for calcium ion and its application to multicolor neuronal imaging. *J. Am. Chem. Soc.* 133:14157–14159. <https://doi.org/10.1021/ja205809h>.

64. Liu, S., C. Lin, ..., P. Zou. 2021. A far-red hybrid voltage indicator enabled by bioorthogonal engineering of rhodopsin on live neurons. *Nat. Chem.* 13:472–479. <https://doi.org/10.1038/s41557-021-00641-1>.
65. Afshar Saber, W., F. M. Gasparoli, ..., M. Antkowiak. 2018. All-optical assay to study biological neural networks. *Front. Neurosci.* 12:451. <https://doi.org/10.3389/fnins.2018.00451>.
66. Soor, N. S., P. Quicke, ..., A. J. Foust. 2019. All-optical crosstalk-free manipulation and readout of Chronos-expressing neurons. *J. Phys. D Appl. Phys.* 52:104002. <https://doi.org/10.1088/1361-6463/aaf944>.
67. Berndt, A., S. Y. Lee, ..., K. Deisseroth. 2016. Structural foundations of optogenetics: determinants of channelrhodopsin ion selectivity. *Proc. Natl. Acad. Sci. USA.* 113:822–829. <https://doi.org/10.1073/pnas.1523341113>.
68. Lin, J. Y., M. Z. Lin, ..., R. Y. Tsien. 2009. Characterization of engineered channelrhodopsin variants with improved properties and kinetics. *Biophys. J.* 96:1803–1814. <https://doi.org/10.1016/j.bpj.2008.11.034>.
69. Kato, H. E., M. Kamiya, ..., O. Nureki. 2015. Atomistic design of microbial opsin-based blue-shifted optogenetics tools. *Nat. Commun.* 6:7177. <https://doi.org/10.1038/ncomms8177>.
70. Wietek, J., and M. Prigge. 2016. Enhancing channelrhodopsins: an overview. *Methods Mol. Biol.* 1408:141–165. https://doi.org/10.1007/978-1-4939-3512-3_10.
71. Lórenz-Fonfría, V. A., B. J. Schultz, ..., J. Heberle. 2015. Pre-gating conformational changes in the ChETA variant of channelrhodopsin-2 monitored by nanosecond IR spectroscopy. *J. Am. Chem. Soc.* 137:1850–1861. <https://doi.org/10.1021/ja5108595>.
72. Bedbrook, C. N., A. J. Rice, ..., F. H. Arnold. 2017. Structure-guided SCHEMA recombination generates diverse chimeric channelrhodopsins. *Proc. Natl. Acad. Sci. USA.* 114. E2624–e2633. <https://doi.org/10.1073/pnas.1700269114>.
73. Bedbrook, C. N., K. K. Yang, ..., F. H. Arnold. 2019. Machine learning-guided channelrhodopsin engineering enables minimally invasive optogenetics. *Nat. Methods.* 16:1176–1184. <https://doi.org/10.1038/s41592-019-0583-8>.